Acta Materialia 113 (2016) 311–319

Contents lists available at ScienceDirect

Acta Materialia

journal homepage: www.elsevier.com/locate/actamat

Full length article

From electronic structure to phase diagrams: A bottom-up approach to understand the stability of titanium–transition metal alloys

Liang-Feng Huang [a, b], Blazej Grabowski [a, *], Jian Zhang [c], Min-Jie Lai [a], C. Cem Tasan [d], Stefanie Sandlöbes [e], Dierk Raabe [a], Jörg Neugebauer [a]

[a] Max-Planck-Institut für Eisenforschung GmbH, 40237 Düsseldorf, Germany
[b] Department of Materials Science and Engineering, Northwestern University, Evanston, IL 60208, United States
[c] State Key Laboratory for Mechanical Behavior of Materials, Xi'an Jiaotong University, Xi'an 710049, China
[d] Department of Materials Science and Engineering, MIT, Cambridge, MA 02139, United States
[e] Institut für Metallkunde und Metallphysik, RWTH Aachen, Kopernikusstr. 14, 52074 Aachen, Germany

ARTICLE INFO

Article history:
Received 1 April 2016
Received in revised form
26 April 2016
Accepted 30 April 2016
Available online 13 May 2016

Keywords:
Titanium alloys
Transition metal
Stability
Phase diagram
Density functional theory

ABSTRACT

We have computed formation energies for all technologically relevant transition metal solutes in the α, β, and ω phases of Ti, employing *ab initio* simulations. We analyze and explain their periodic-table trends, and from their differences we derive stabilization energies which provide direct insight into phase stabilization effects of the various solutes with respect to α, β, and ω. This allows us to identify strong β stabilizers in the middle of each electronic *d* shell in consistency with experimental knowledge. Based on an extension of the stabilization energies to free energies we derive a wide range of Ti-transition metal phase diagrams. A detailed comparison to available experimental martensitic transformation temperatures and to measurements performed in this study shows that, despite some quantitative discrepancies, the qualitative trends can be expected to be correct. An important feature that is displayed by a limited range of the computed phase diagrams is a triple point at which the three phases, α, β, and ω, meet. This insight provides a plausible explanation for the complexity observed in gum metals, a class of Ti alloys with very special materials properties.

1. Introduction

Titanium alloys are widely applied as structural materials in aerospace and biomedicine, due to their variable elastic modulus, excellent corrosion and wear resistance, light weight, good ductility, and high biocompatibility [1–6]. To satisfy the increasing technological and industrial requirements, the mechanical, thermodynamic, and chemical properties of Ti alloys continue to be under intensive experimental and theoretical investigation, with the goal of achieving highly optimized material properties.

Transition metals (TMs) are among the most important alloying elements in Ti alloys, because their *s*, *p*, and *d* electrons can have profound influence on various properties. For example, it is well known that the elastic modulus, plasticity, and shape memory behavior can be effectively tuned by TM additions [1–4,7–15]. A crucial ingredient enabling this versatile behavior are the three phases α, β, and ω [16,17], the stabilities of which can be effectively tuned by the TM solutes. The details of the phase stabilities and the resulting mechanical properties of the Ti alloys critically depend on the atomic number of the added TM atoms [1,2,18–23]. This is typically explained using approximate empirical correlations with the electron valence number [24–30]. However, these empirical correlations can be invalid [20,31–35], and thus further explicit investigations are required to better understand the phase stability dependencies for complementing experimental data.

In this work, a bottom-up approach rooted in *ab initio* simulations is used to reveal the periodic-table trends in the stabilities of the α, β, and ω phases in all technologically relevant Ti–TM alloys. We employ density functional theory to compute the formation and stabilization energies of all the TM solutes in the three Ti phases. Investigating the stabilization energies provides clear trends as a function of the electron valence number that can be explained in terms of a coordination-number argument in conjunction with a simple bonding model. Extending the stabilization energies to free energies enables us to compute a wide range

* Corresponding author.
E-mail address: b.grabowski@mpie.de (B. Grabowski).

http://dx.doi.org/10.1016/j.actamat.2016.04.059

of Ti–TM phase diagrams that we carefully validate by comparing with experimentally available martensitic transformation temperatures from literature and as obtained in this study. Finally, we apply the computed phase diagrams to analyze the complex deformation behavior in gum metals, a special class of Ti alloys with promising properties.

2. Methodology

2.1. Computation of the TM solute formation energy

A central quantity determining phase stabilities in Ti–TM alloys is the formation energy, E_X^a, defined as

$$E_X^a = E_{n\mathrm{Ti}+X}^a - nE_{\mathrm{Ti}}^a - \mu_X, \tag{1}$$

where a is an index running over the three phases α, β, and ω, X is an index running over all TM solutes, $E_{n\mathrm{Ti}+X}^a$ is the total energy of a supercell in phase a with n Ti atoms and with one substitutional TM atom, E_{Ti}^a is the total energy per atom of a pure Ti supercell in phase a, and μ_X is the chemical potential of the TM solute. The formation energy in Eq. (1) measures the energetic preference of a TM solute to dissolve in one of the Ti phases α, β, or ω with respect to the chemical potential μ_X. A negative formation energy indicates that the reaction is exothermic and thus that the incorporation of the TM solute will take place.

A typical choice to reference the chemical potential μ_X are the stable bulk phases of the alloyed elements (e.g., hcp for Zr, bcc for Mo, or fcc for Ag). However, for the present purpose of revealing chemical trends of alloying to the Ti matrix, the stable bulk phases are not a good reference because of the strongly varying interatomic bonding across the d series. A more suitable choice are the energies of the isolated TM atoms (in particular after subtracting the contribution due to atomic magnetism, cf. Fig. 1 below), revealing clear chemical dependencies and trends. It should be noted that for phase stabilities the choice of the chemical potential is not critical as it cancels from the corresponding energy differences.

For determining phase stabilities we consider in particular formation-energy differences according to

$$E_X^{a-b} = \left(E_X^a - E_X^b\right) - \left(E_{\mathrm{Ti}}^a - E_{\mathrm{Ti}}^b\right), \tag{2}$$

where a and b (with $a \neq b$) are indices running over the phases α, β, and ω. By subtracting the term $(E_{\mathrm{Ti}}^a - E_{\mathrm{Ti}}^b)$ in Eq. (2) we have excluded the intrinsic energy difference between the a and b phases of pure Ti. Doing so, E_X^{a-b}, which we will call *stabilization energy*, becomes a useful descriptor having a one-to-one correspondence to the strength with which a TM solute stabilizes a certain phase (e.g., whether it is a β stabilizer).

The computation of the formation energy, E_X^ω, for the ω phase is complicated by the fact that this phase has two symmetrically inequivalent sublattices. The corresponding sites are the trigonal, ω_1, and the honeycomb, ω_2, site corresponding to 1/3 and 2/3 of all ω lattice sites, respectively. To take this properly into account, we have computed the formation energies for both sites, $E_X^{\omega_1}$ and $E_X^{\omega_2}$, for all TM solutes from which we then determined

$$E_X^\omega = \frac{1}{3}E_X^{\omega_1} + \frac{2}{3}E_X^{\omega_2}, \tag{3}$$

corresponding to the averaged formation energy in ω for fully randomly distributed TM solutes. Experimentally the average in Eq. (3) represents a rapid quenching from the high temperature β to the low temperature ω field, for which the TM solutes are kinetically hindered to redistribute to the more favorable sites and to form ordered intermetallic phases.

The computation of the formation energy, E_X^β, for the β phase is complicated by the fact that this phase is dynamically unstable in pure Ti at low temperatures [36–39]. As a consequence, introducing a TM solute leads to local relaxations away from the bcc lattice sites. In a real system, these local relaxations are removed at finite temperatures where phonon-phonon interactions are able to stabilize the system on the bcc lattice positions. Since an explicit treatment of phonon-phonon interactions is computationally prohibitive for a wide composition range investigation, we have employed a computational trick as utilized previously in Ref. [40]: In the β phase only the coordination neighbors of the solute are allowed to relax (coordination-neighbor relaxation). This coordination-neighbor relaxation ensures that all atoms remain close to their bcc lattice positions, but it still provides enough flexibility to release the main portion of the relaxation energy.

All formation energies E_X^a were calculated using density functional theory as implemented in the VASP code [41]. The projector augmented wave method [42,43] was used to describe the electronic wavefunctions, and the PBE [44] functional for the electronic exchange and correlation. Spin polarization was included for the magnetic elements. Supercells of $5 \times 5 \times 3$, $4 \times 4 \times 4$, and $3 \times 3 \times 5$ times the conventional α, β, and ω unit cells were employed for the TM solute supercell calculations. A k-point grid of $5 \times 5 \times 5$ was

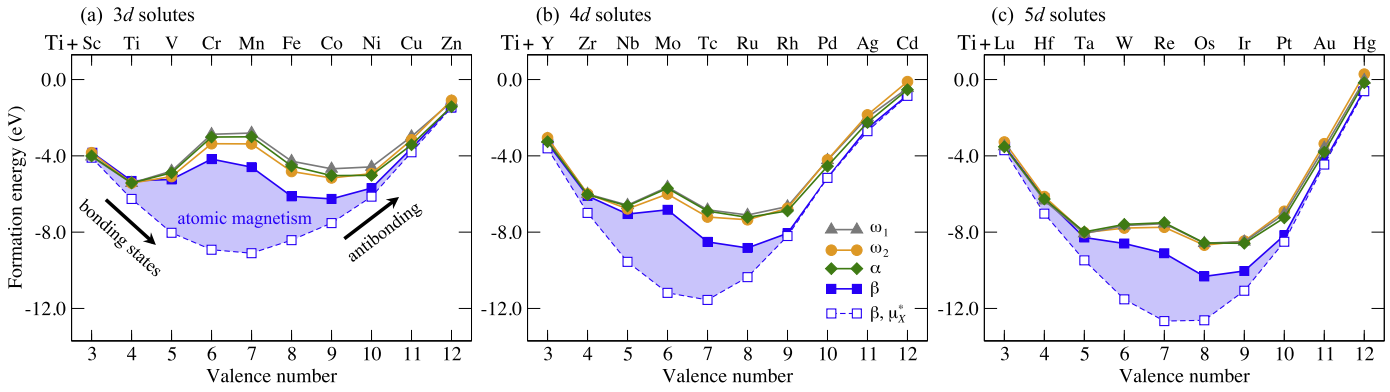

Fig. 1. *Ab initio* computed formation energies of all (a) 3*d*, (b) 4*d*, and (c) 5*d* TM solutes in α, β, and ω Ti according to Eq. (1). For ω, formation energies for each of the symmetrically inequivalent sites, ω_1 and ω_2, are shown. For β, an additional formation energy is shown (blue open squares and dashed line) for which a modified, non-magnetic chemical potential μ_X^* was used in Eq. (1) that excludes the effect of atomic magnetization (blue shaded area). (For interpretation of the references to colour in this figure legend, the reader is referred to the web version of this article.)

used for the integration of electronic states in the Brillouin zone in all supercells, together with the Methfessel-Paxton smearing technique [45] with an energy width of 0.1 eV. An energy cutoff of 400 eV was employed for the plane wave basis.

2.2. Computation of Ti–TM phase diagrams

To enable the computation of Ti–TM phase diagrams, the stabilization energy from Eq. (2) needs to be extended to concentration and temperature dependent free energy differences. However, computing the complete free energy surface fully from *ab initio* is a tremendous computational task even for a single binary system. Therefore, for the here performed wide-range investigation of all Ti–TM phase diagrams, a properly chosen approximate treatment is unavoidable. To this end, a computationally efficient approach that can be expected to capture the relevant physics is the following.

Using the stabilization energy defined in Eq. (2) we can determine the concentration dependence of the alloy energy using a linearized approximation of the phase stabilities by

$$E^{a-b}_{\mathrm{TiX}}(x) = \left(E^{a}_{\mathrm{Ti}} - E^{b}_{\mathrm{Ti}}\right) + xE^{a-b}_{X}, \tag{4}$$

where x is the TM solute concentration. In Eq. (4) the TM solutes alloyed to the Ti matrix are assumed to be non-interacting. To determine the temperature dependence we next extend to free energy differences according to

$$F^{a-b}_{\mathrm{TiX}}(x,T) = E^{a-b}_{\mathrm{TiX}}(x) + F^{a-b}_{\mathrm{el}}(T) + F^{a-b}_{\mathrm{vib}}(T), \tag{5}$$

where F^{a-b}_{el} and F^{a-b}_{vib} are the electronic and vibrational free-energy differences between phase a and b at temperature T, approximated by the corresponding free energy contributions in pure Ti. In particular, we used the finite temperature extension to density-functional-theory [46] to compute the electronic free energy and the Debye-Grüneisen approximation [47] to obtain the vibrational free energy. For the latter we used the Debye temperatures as derived in Ref. [36]. A configurational entropy difference is not required in Eq. (5) because, for the assumed equal distribution of non-interacting TM solutes, all phases acquire the same configurational entropy.

An analysis of $F^{a-b}_{\mathrm{TiX}}(x,T)$ allows us to determine the phase with the lowest free energy as a function of solute concentration and temperature. This gives direct access to all Ti–TM phase diagrams and thereby enables a wide composition range investigation of periodic table trends for Ti alloys. We expect the computed trends to be a realistic representation of experiment despite the involved approximations. For example, in a previous work on Ti–Nb and Ti–Mo alloys [48], we showed that the linear assumption in Eq. (4) is a good approximation even up to solute concentrations of $\approx$40 at.%. Further, for Ti_3Nb it was shown [49] that, for fully optimized structures, the energy only varies within a couple of meV/atom for different arrangements of Nb atoms, indicating a weak solute-solute interaction. In general, one can expect relatively weak solute-solute interactions for the early TM columns (i.e., Sc, Ti, V, and Cr columns), which are known to form solid solution phases with Ti over large compositional ranges [1–3,16]. For the later TM columns (i.e., Mn, Fe, Co, Ni, Cu, and Zn) various ordered intermetallic phases are known to form [1,2,16,50] indicating stronger solute-solute interactions. We will consider this fact in more detail in the interpretation of the computed phase diagrams in Sec. 4.1 and present further validation of our *ab initio* results by comparing them with available experimental data from literature and with our new measurements as introduced in the next section.

2.3. Experimental techniques

Ti–Mo, Ti–Fe, and Ti–V alloys with compositions as shown in Table 1 were prepared by electric arc melting under Ar atmosphere and cast into a copper mould. The as-cast billets were deformed by hot swaging in the β phase region at 975° C to a thickness reduction of 50%. The lattice parameters of the alloys were determined by X-ray diffraction (Philips PW3020 diffractometer, Cu-Kα) using Rietveld refinement. Transformation temperatures were determined by differential thermal analysis (DTA) in a Setaram SETSYS-18 DTA using a rate of 10 K/min. The annealed and furnace cooled specimens revealed martensitic microstructures for the investigated alloys.

3. Results of the *ab initio* wide-range study

3.1. Zero temperature formation energies of all TM solutes

Fig. 1 presents the *ab initio* computed formation energies of all TM solutes in the three phases of Ti α, β, and ω (filled symbols and solid lines). For ω, the two inequivalent sites ω_1 and ω_2 are shown. We observe that in all phases and for all d shells (3d, 4d, and 5d) the formation energy follows a W-shaped dependence as a function of the electron valence number. Interestingly, the intermediate peaks in the curves at valence numbers 6 and 7 are not related to the incorporation of the TM solutes into the Ti matrix. They are instead an artefact of the employed chemical potential μ_X in Eq. (1), for which we have used an isolated TM atom. For a d shell that is close to half occupation (i.e., valence numbers 6 and 7) isolated TM atoms acquire a strong atomic magnetization. When the corresponding contribution is subtracted, a nicely parabolic dependence is obtained for the formation energies of all phases, as exemplified for the β phase by the blue dashed lines in Fig. 1.

The trends observed in Fig. 1 for the TM formation energies in Ti are explored for the first time in this study. However, similar periodic table trends are well-known for cohesive energies of elemental TMs [51–55]. The parabolic dependence after subtraction of the atomic magnetization has also been investigated previously and it can be explained within the simplified Friedel model for the bond energy of d electrons [56]. According to this model, for valence numbers below 6 the bonding states of the d shell are populated, and thus increasing the number of electrons considerably strengthens the bonds [57]. For larger valence numbers, the anti-bonding states of the d shell are populated, and increasing the number of electrons results in a weakening of the valence-bond strength [cf. arrows in Fig. 1(a)].

The absolute formation energies displayed in Fig. 1 are well suited for revealing general chemical trends, but for determining phase stabilities we need to consider their differences, specifically the stabilization energy according to Eq. (2) and as displayed in Fig. 2. Focussing first on the $\alpha - \beta$ stabilization energy [Fig. 2(a)], we observe a close-to-parabolic dependence with valence number, which is similar for each d shell (3d = blue solid, 4d = red dashed, 5d = green dotted line). For valence numbers 3 and 4, i.e., smaller than or equal to the one of Ti, the stabilization energy is comparatively small. For larger valence numbers the stabilization energy strongly decreases—almost down to values of −1.8 eV—which reveals a strong β stabilizing effect of TM elements in the middle of each d shell. The β stabilizing effect becomes smaller towards the end of the d shells. For Cr, Mn, and Fe from the 3d shell, a change in the stabilization energy can be observed when magnetism inside the TM solute supercell is considered (open *versus* filled blue circles; note that this magnetism differs from the atomic magnetism). Other TM solutes do not induce magnetism inside the Ti matrix within the considered non-interacting limit.

Table 1
Nominal and effective concentrations (obtained with wet chemical analysis) of the transition metal solutes in the investigated Ti alloys.

	Ti–Mo			Ti–Fe			Ti–V		
Nominal (wt.%)	1	2	3	1	2	3	1	2	3
Nominal (at.%)	0.50	1.00	1.50	0.86	1.71	2.57	0.94	1.88	2.82
Wet chemical analysis (at.%)	0.50	0.94	1.52	0.96	1.62	2.63	1.02	2.08	2.95

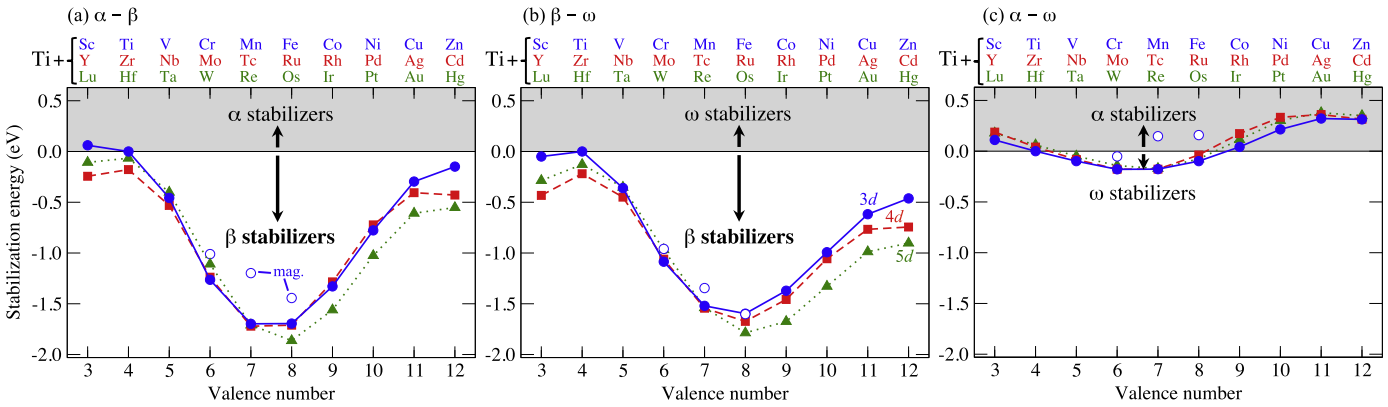

Fig. 2. Stabilization energies (a) $E_X^{\beta-\alpha}$, (b) $E_X^{\beta-\omega}$, and (c) $E_X^{\omega-\alpha}$ for all TM solutes calculated according to Eq. (2). For the 3*d* elements Cr, Mn, and Fe, non-magnetic results are shown by the blue filled circles and solid lines, whereas the magnetic results are indicated by the open circles. 'Magnetic' refers here to the magnetism induced inside the Ti matrix and not to the atomic magnetism indicated in Fig. 1, which cancels in the present figure. (For interpretation of the references to colour in this figure legend, the reader is referred to the web version of this article.)

The $\alpha - \beta$ stabilization energy observed in Fig. 2(a) can be explained utilizing recent insights about the importance of the coordination number in pure Ti [40]. In pure Ti, the α phase has an optimum coordination number of 12 resulting in strong bonds, while the β phase is under-coordinated with a coordination number of 8, resulting in weak bonds. This difference in coordination number is the origin of the low temperature phase stability of the α phase in pure Ti. However, the picture changes when TM solutes are introduced that provide additional electronic bonding states (i.e., valence numbers larger than Ti). Introducing such a TM solute into the β phase can easily perturb the Ti electronic states and form additional nearest-neighbor bonds around the solute. The alloyed β phase is thereby considerably stabilized with respect to the pure Ti β phase. TM solutes incorporated into the α phase have a much smaller effect because the pure Ti α phase is already very stable. The close-to-parabolic dependence can be understood by combining the coordination number argument with the Friedel model mentioned above, i.e., those additional bonding states introduced by the TM solutes into the β phase are occupied first followed by the anti-bonding states.

The $\beta - \omega$ stabilization energy [Fig. 2(b)] is similar to the $\alpha - \beta$ one. The explanation based on the coordination number difference can be likewise transferred, because the ω phase has an average coordination number of 12 [40], i.e., the same as the α phase. The ω phase is therefore already very stable for pure Ti, and addition of TM solutes cannot lead to a further stabilization, in contrast to the alloyed β phase. The same reasoning explains why the $\alpha - \omega$ stabilization energy is rather small [Fig. 2(c)]: Both, α and ω, are very stable and close in energy for pure Ti, and addition of TM solutes has only a minor effect. In summary, we can conclude from our wide-range analysis of the *ab initio* formation energies that most TM solutes strongly stabilize the β phase over both the α and ω phase, i.e., they are β stabilizing elements.

An interesting by-product of our study is displayed in Fig. 3, which highlights the local geometrical changes around the 3*d* TM solutes as an example. In particular, we plot the distortion of the nearest neighbor bonds induced around the solutes. In consistency

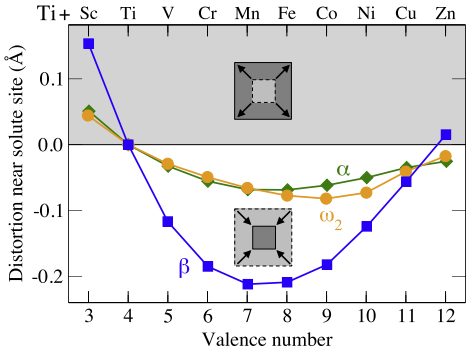

Fig. 3. Distortion of the nearest-neighbor bonds around the 3*d* solutes in the three Ti phases. For ω, the distortions around the honeycomb site, ω_2, are only shown, because the distortions around the ω_1 site are similar. Negative values correspond to compression and positive values to expansion as indicated by the two insets.

with the formation energies, we observe that the β phase has the strongest impact on the bonds which are reduced even by −0.2 Å in the middle of the *d* shell. Interestingly, our X-ray diffraction measurements also revealed reduced lattice spacings for the experimentally investigated alloys when compared to pure Ti. In agreement with the simulations, the β phase experiences a higher volume contraction than the α phase. Further, the experiments showed that this effect is highest for Fe followed by V and least for Mo, in good agreement with the simulation results (Fe: −0.21 Å, V: −0.12 Å, Mo: −0.11 Å). Such strong local lattice distortions might have an influence on dislocation glide, thereby affecting plasticity in Ti alloys.

3.2. Extension to finite temperatures: Ti–TM phase diagrams

Using the stabilization energies from the previous section and the extension to free energies according to Eq. (5), we have computed Ti–TM phase diagrams for all TM solutes as displayed in

Fig. 4. In the shown phase diagrams we have suppressed the possibility of phase separation, i.e., the diagrams correspond to metastable and not to equilibrated conditions. A large part of the displayed α phase field (yellow region) would therefore be labelled α' or α'' (depending on the solute concentration) in experimental terminology, but for consistency with the previous discussion we keep the label α. The metastable representation of the phase diagrams is particularly suited for analyzing rapidly cooled Ti alloys.

Focussing first on the Ti–Ti phase diagram, i.e., just pure Ti (second in the first row), we observe the well-known fact that above $\approx$1050 K the β phase (red shaded area) is the most stable one, and that it transforms to the α phase (yellow area) upon cooling below this temperature. At very low temperatures ($\approx$100 K) the ω phase (blue area) becomes more stable than the α phase. Employing this Ti–Ti diagram and additionally the stabilization energies from Fig. 2, all other Ti–TM phase diagrams can be understood. For the discussion, it is particularly convenient to start with a specific *d* shell, and we will take the 5*d* shell (bottom row) for that purpose.

For the TM solutes Lu and Hf with valence numbers smaller than or equal to Ti, we see a moderate change of the β to α transformation temperature with solute concentration (boundary between red and yellow region). Increasing the valence number, i.e., going to Ta, W, etc., the β to α transformation temperature decreases more and more rapidly with solute concentration. As a consequence, the stability range of the β phase becomes very large in particular for Re and Os. Towards the end of the 5*d* series the transformation temperature again becomes less steep with solute concentration. These changes in the transformation temperature exhibit a one-to-one correspondence with the $\alpha - \beta$ stabilization energy for the 5*d* solutes [green dashed line in Fig. 2(a)]: The more negative the stabilization energy is (like for the elements in the middle of the 5*d* row) the steeper is the dependence of the transformation temperature with solute concentration. The curvature in the transformation temperature (see, e.g., deviation from the straight dashed line for the Hg phase diagram) is due to the curvature in temperature dependence of the vibrational free-energy differences in Eq. (5).

The α to ω and the β to ω transformation temperature dependencies can be understood in an analogous fashion. The α to ω transformation temperature (boundary between yellow and blue region) decreases with solute concentration for Lu and Hf, and also for Ir, Pt, Au, and Hg, resulting in a very small ω phase field region for these elements. The origin of the decrease is the corresponding positive $\alpha - \omega$ stabilization energy [Fig. 2(c)]. For the other elements, Ta, W, Re, and Os, the stabilization energy is negative, and consequently the α to ω transformation temperature increases with solute concentration. Only for these elements (Ta, W, Re, Os) a phase boundary between β and ω (boundary between red and blue) occurs in the respective phase diagrams. The solute dependence of the β to ω transformation temperatures is very similar to the dependence of the β to α transformation temperatures (i.e., strongly decreasing) due to a similar stabilization energy [Fig. 2(a) *versus* (b)]. An interesting consequence of the three phase boundaries in Ta, W, Re, and Os, is that a triple point exists where all three phases meet as highlighted for W in Fig. 4.

The Ti–TM phase diagrams for the 4*d* solutes (middle row in Fig. 4) have the same characteristics as the ones for the 5*d* solutes. Employing the non-magnetic stabilization energies for Cr, Mn, and Fe also the 3*d* solutes produce phase diagrams that follow the same trends. This can be seen in the upper row of Fig. 4 when considering the dashed transformation temperatures for Cr, Mn, and Fe. Taking magnetism into account, the phase diagram of Ti–Cr is only slightly affected, but the phase diagrams of Ti–Mn and Ti–Fe experience more significant changes. In particular the ω phase field is strongly suppressed resulting in the disappearance of the triple point.

4. Validation and application of the results

4.1. Experimental validation of the ab initio results

In order to assess the accuracy of the computed *ab initio* phase diagrams, we provide in this section a comparison to available experimental results from literature and results obtained in this study.

Generally, it is well known that TM solutes stabilize the Ti β phase and that the stabilization is strongest for solutes in the middle of each *d* shell [1–3,16,48]. This β stabilizing effect is reflected by the calculated close-to-parabolic stabilization energies [Fig. 2(a) and (b)] and the resulting dominance of the β phase field in the Ti–TM phase diagrams [red region in Fig. 4]. Zr and Hf (same valence number as Ti) have been instead traditionally considered as *neutral* solutes in Ti [1], in the sense that their addition does not influence the β to α transformation temperature. Only recent X-ray diffraction measurements in Ti–NbZr/Hf, Ti–TaZr/Hf, and Ti–NbTaZr/Hf alloys [10,58–60] have revealed that Zr and Hf are in fact weak β stabilizers. These measurements are consistent with our simulated results which confirm that Zr and Hf have a weak β stabilization effect: The β to α transformation temperature decreases by about $-$200 K per 10 at.% solute concentration for Zr, and by $-$100 K per 10 at.% for Hf.

For a more quantitative evaluation, we need to compare with experiments that investigate phase transitions and transformations in quenched Ti alloy samples. Lütjering [2], for example, has compiled various results for the critical solute concentrations at which the high temperature β phase is retained after quenching. These experimental concentrations can be compared with the computed metastable transformation concentrations at room temperature, as done in Fig. 5. Overall we observe a reasonable agreement between experiment and theory, quantifying the β stabilization effect for TM solutes with valence numbers larger than Ti. However, for the group V elements (V, Nb, Ta) there appears to be a discrepancy regarding the dependence on the *d* shell. Theory predicts the smallest critical concentration for Nb, whereas experiment indicates the opposite, i.e., that Nb has the largest critical concentration. To put this apparent discrepancy into perspective one needs to consider that the experimental values are subject to rather significant scatter, as for example induced by locally heterogeneous solute concentrations resulting from segregation during solidification. Further, the diffusion rates of the different TM solutes have to be considered: A fast diffusing element might segregate during quenching and, hence, locally stabilize the β phase due to partitioning.

Fortunately, for some TM solutes more detailed experimental investigations are available that assessed the dependence of the martensitic transformation temperature as a function of concentration. Fig. 6 shows a comparison of the simulated and experimental phase boundaries for Ti–Ta, Ti–Nb, and Ti–Mo alloys [18,61–64]. From the experimental data in Fig. 6(b) it is clear that Nb is a stronger β stabilizer than Ta, in consistency with our theoretical prediction [Fig. 6(a)], but in contrast to the experimental data based on the retained β phase analysis (Fig. 5). Fig. 6(b) also reveals experimental scatter for the Ti–Mo system which is due to different measurement techniques—TEM and the Hall effect (filled and half-filled triangles) and resistance measurements (open triangles). Nevertheless, the comparison in Fig. 6 allows us to conclude that the trend in the transformation temperatures is correctly predicted by theory, giving the following sequence: Ti–Mo < Ti–Nb < Ti–Ta. Quantitatively, we observe differences with respect to experiment, for example, the Ti–Ta transformation

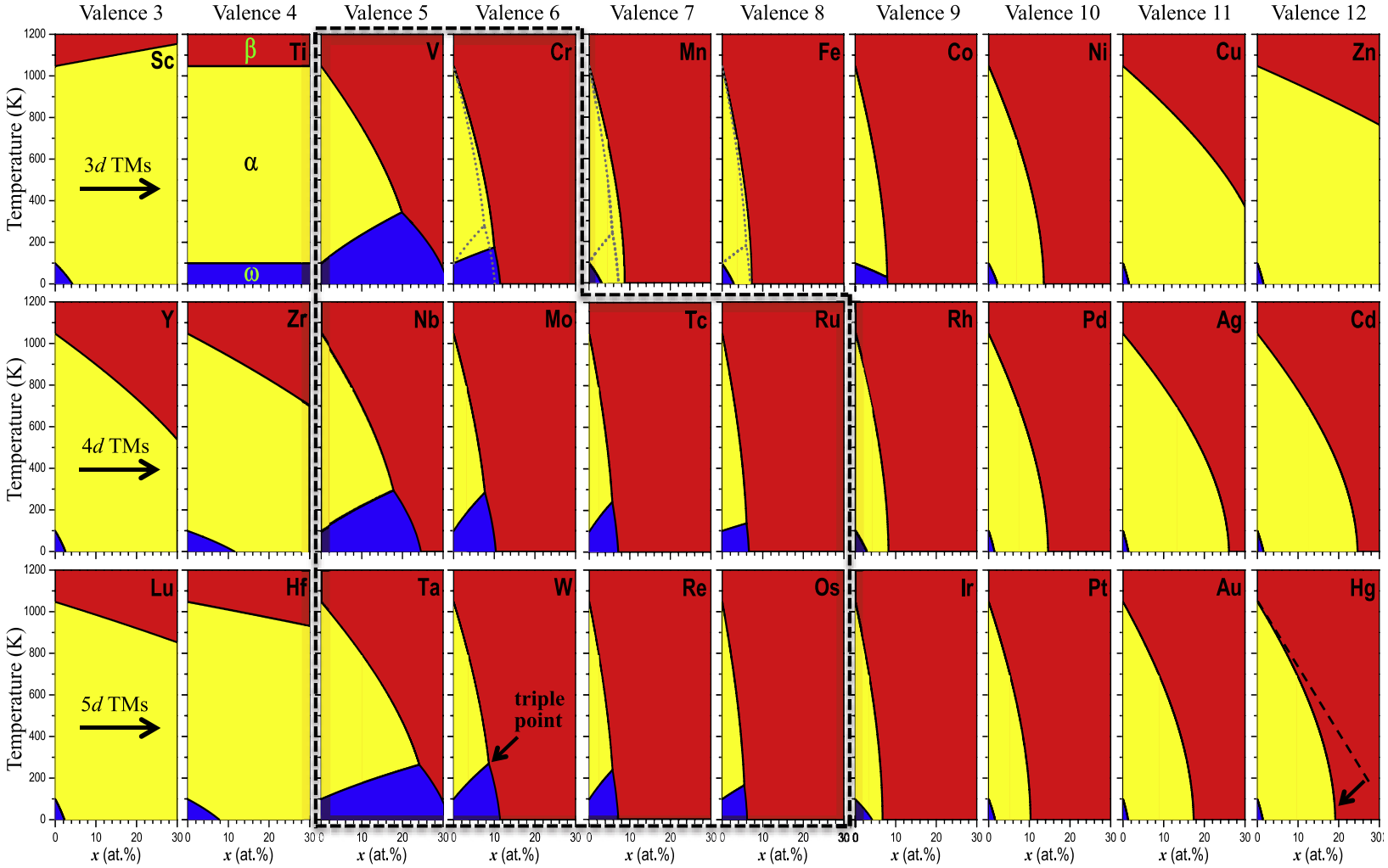

Fig. 4. Metastable phase diagrams of Ti–transition metal (TM) alloys computed from *ab initio*. Three phases are present: α (yellow region), β (red), and ω (blue). In experimental terminology, the displayed α phase field corresponds to a large part to the α' or α'' phase, i.e., to the hcp or tetragonally distorted hcp phase obtained after quenching from the β phase field below the martensitic transformation temperature. The phase diagrams highlighted by the black dashed lines contain the special feature of a triple point at which the three phases meet as indicated for W. For the Ti–Cr, Ti–Mn, and Ti–Fe alloys, non-magnetic phase diagrams are indicated by grey dotted lines, whereas the colored phase diagrams correspond to the experimentally representative magnetic situation. (For interpretation of the references to colour in this figure legend, the reader is referred to the web version of this article.)

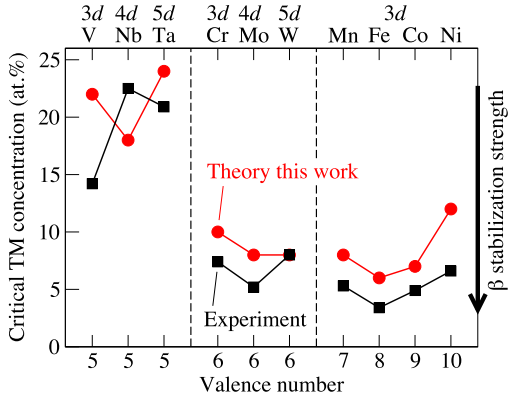

Fig. 5. Comparison of experimental critical concentrations from Ref. [2] (black squares) at which a retained β phase is still observed after quenching to room temperature with theoretical transformation concentrations (red circles) obtained at room temperature from the metastable phase diagrams in Fig. 4. Smaller concentrations indicate a stronger β stabilization effect. (For interpretation of the references to colour in this figure legend, the reader is referred to the web version of this article.)

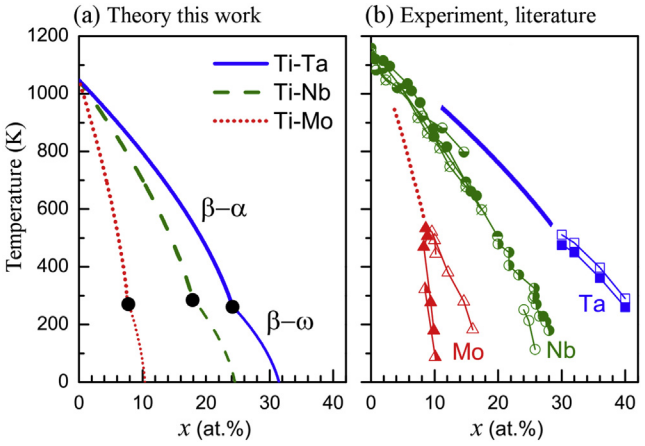

Fig. 6. (a) Simulated $\beta - \alpha$ and $\beta - \omega$ phase boundaries with the triple point indicated by the black dots, and (b) experimentally determined martensitic boundaries from literature [18,61–64] in Ti–Ta, Ti–Nb, and Ti–Mo alloys.

concentration at room temperature is 25 at.% in theory, but 40 at.% in experiment. The discrepancy becomes smaller for the strong β stabilizer Mo, for which theory predicts about 8 at.% and experiment a range of 8 at.%–14 at.% depending on the measurement technique. This quantitative underestimation of the experimental temperatures is probably due to the omission of the concentration dependence of the free energy contributions in Eq. (5).

In order to extend the quantitative evaluation of our *ab initio* results we have performed additional measurements in this study. As displayed in Fig. 7(b), we focussed in particular on a smaller Mo concentration window as compared to the experimental data shown in Fig. 6(b) and additionally on the Ti–Fe and Ti–V systems. We observe the same trends in the transformation temperatures as predicted by *ab initio*, i.e., Ti–V > Ti–Mo ≈ Ti–Fe. Further, when linearly rescaling the theoretically predicted transformation temperatures good quantitative agreement with the experimental transformation temperatures is found, Fig. 7.

From our theoretical transformation temperatures we can straightforwardly determine whether the β phase has transformed to the α or to the ω phase. This is highlighted in Fig. 6(a) by the black dots which separate the β to α transformation (above) from the β to ω transformation (below). Such a separation cannot be directly extracted from the experimental curves in Fig. 6(b). Additional

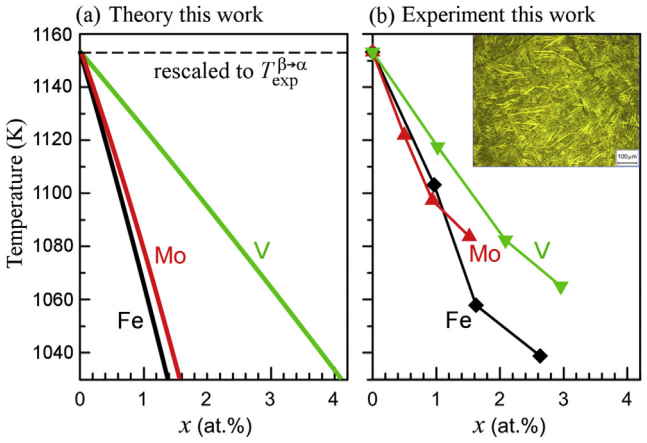

Fig. 7. (a) Simulated $\beta - \alpha$ phase boundaries and (b) experimentally measured martensitic boundaries in Ti–Fe, Ti–Mo, and Ti–V alloys. To enable a comparison, the theoretical boundaries in (a) have been linearly rescaled to match the experimental β to α transformation temperature, $T_{exp}^{\beta\to\alpha}$, of pure Ti. In (b), the inset shows the martensitic microstructure obtained after quenching for a Ti-0.94 at.% Mo alloy.

information on the microstructure after transformation is required and we can utilize experiments performed by Devaraj et al. [65] on Ti–Mo for that purpose. The authors of Ref. [65] have investigated the microstructure of a Ti 9 at.% Mo alloy after quenching and they clearly revealed the presence of ω phase particles. From our metastable phase diagram for Ti–Mo [red dotted curve in Fig. 6(a)] we see that the triple point where the three phases meet (black dot) is close to a concentration of 8 at.% Mo. For higher concentrations (as in the study of Ref. [65]) the ω phase can be therefore indeed expected to form after quenching to room temperature. Note however that theory and experiment do not fully match in quantitative terms, because the theoretical transformation temperatures are somewhat too low. This might be caused by the involved theoretical approximations, but also by experimental imperfections such as for example impurity concentrations that modify the transformation temperatures.

Summarizing the validation of our results, we can expect quantitative differences between the theoretical and experimental phase boundaries. These quantitative differences should become smaller for TM solutes that are strong β stabilizers because the involved theoretical approximations are less severe for such systems. Qualitatively, we can expect the theoretical phase boundaries to be a faithful representation of the trends for the various investigated TM solutes. It should be noted, however, that within the employed approximation of non-interacting solutes (Sec. 2.2) we are unable to describe sublattice ordering and thus the formation of intermetallic phases on the investigated lattices such as, e.g., $D0_3$ for bcc or $D0_{19}$ for hcp. Intermetallic phases on other lattices are likewise invisible within our approach. Intermetallic phases can be expected to form in particular for the later TM columns starting at a solute concentration of ≥25 at.%, e.g., Ti_3Cu, Ti_3Au, Ti_3Hg, Ti_3Pt, and corresponding phase diagrams (Fig. 4) should be, thus, used with caution.

4.2. Application to gum metals: triple point as a source of complexity

'Gum metals' are a class of β titanium-based alloys [66–68], which possess an excellent yet unusual mechanical behavior: At room temperature, when deformed in tension, gum metals exhibit a high yield stress (up to 1 GPa [68,69]) and very high elongation to failure (up to 35% [70]), surprisingly at very low strain hardening.

Despite the interest in this alloy class, the physical mechanisms governing the plastic behavior are still unclear. It appears however that an important condition is a careful choice of the main alloying element and its specific concentration. Most prominent in this respect is the Ti–Nb system with typical concentrations of 23 at.% Nb.

In early experimental studies on gum metals with a composition of Ti-23Nb-0.7Ta2Zr-1.2O at.% [66,68], it was found that the generation of the so-called giant faults determines plastic deformation, while phase transformations and dislocation slip have not been observed. In contrast, follow-up experimental studies identified a variety of plastic deformation modes in gum metals with similar chemical compositions: e.g., nanodisturbances [71], dislocations [31,70,72–75], twining, phase transformations (β to α and β to ω) [28,69,76–79], and even the involvement of all these deformation modes in one sample [80]. Which deformation mode (e.g., twinning, phase transformation, or dislocation slip) dominates the plastic deformation of a Ti gum metal very sensitively depends on the phase composition and stability [8,81–84]. Close to the martensitic phase boundary, this dependence is most pronounced [8,81].

Utilizing our Ti–Nb metastable phase diagram, we can provide a plausible explanation for the origin of the complexity in gum metals. Referring to the simulated phase boundaries of Ti–Nb in Fig. 6(a) (green dashed line) we see that the triple point where α, β, and ω meet (black dot) is close to room temperature and to a concentration of 18 at.% Nb. Considering the above discussed fact that the theoretical Ti–Nb phase boundaries underestimate the experimental ones with respect to solute concentration [Fig. 6(b)], we can conclude that the triple point is very close to the typical gum metal concentration of Ti-23 at.% Nb. This explains the variety of deformation modes experimentally observed in Ti–Nb gum metals, because—due to the vicinity of the gum-metal composition to the triple point—even minute variations in solute concentration, interstitial distribution, or processing history of an alloy can have significant effects on phase composition and, thus, consequently on the mechanical properties.

Based on this insight and with reference to the wide range of metastable phase diagrams displayed in Fig. 4, we can propose a set of candidate TM solute elements that have the potential to replace Nb as the basis alloying element in gum metals. The corresponding phase diagrams are required to exhibit a triple point between α, β, and ω and this is only possible for elements that produce a specific combination of stabilization energies as discussed in Sec. 3.2. This condition is fulfilled for V and Cr from the 3*d* elements with Mn and Fe being ruled out due to magnetism; for Nb, Mo, Tc, and Ru from the 4*d* elements; and for Ta, W, Re, and Os from the 5*d* elements. The corresponding phase diagrams are highlighted in Fig. 4 by the black dashed lines.

5. Conclusions

Employing a bottom-up approach based on *ab initio* calculations we have computed and analyzed formation and stabilization energies of transition metal solutes in the three relevant Ti phases α, β, and ω. From the stabilization energies we have derived a wide range of metastable phase diagrams of Ti-transition metal alloys. Such metastable phase diagrams are well suited for analyzing rapidly quenched systems as often utilized in the design of Ti alloys. We have assessed the accuracy of the computed phase diagrams by comparison to experimental martensitic transformation temperatures: The trends for the various transition metal solutes are well reproduced and the elements in the middle of each *d* shell are clearly identified as strong β stabilizers. Differences with respect to experiments must be expected in absolute values due to the presently unavoidable approximations. For systems where experimental data are available we have quantified these differences (Fig. 6) and we found that the discrepancy becomes smaller for strong β stabilizers. By performing additional measurements, we have extended the quantitative comparison to small concentrations for Ti–Mo, Ti–Fe, and Ti–V, strengthening thereby the confidence in our *ab initio* results. Finally, we have applied the computed phase diagrams to an analysis of gum metals, and we propose that the complexity in the deformation behavior—which is responsible for the outstanding materials properties of these alloys—is related to the triple point at which the α, β, and ω phase fields meet in the phase diagrams. Based on this insight we were able to identify a set of potential gum metal systems: Ti–V, Cr, Nb, Mo, Tc, Ru, Ta, W, Re, Os.

Acknowledgement

The funding by the European Research Council (ERC) under the EU's 7th Framework Programme (FP7/2007-2013)/ERC Grant agreement 290998 and by the ERC under the EU's Horizon 2020 Research and Innovation Programme (Grant No. 639211) is gratefully acknowledged.

References

[1] C. Leyens, M. Peters, Titanium and Titanium Alloys. Fundamentals and Applications, Wiley-VCH, Weinheim, 2003.
[2] G. Lütjering, J.C. Williams, Titanium, Springer, Berlin, 2007.
[3] D. Banerjee, J.C. Williams, Perspective on titanium science and technology, Acta Mater. 61 (2013) 844–879.
[4] M. Geetha, A.K. Singh, R. Asokamani, A.K. Gogia, Ti based biomaterials, the ultimate choice for orthopaedic implants - a review, Prog. Mater. Sci. 54 (2009) 397–425.
[5] M. Niinomi, Recent metallic materials for biomedical applications, Metall. Mater. Trans. A 33A (2002) 477–486.
[6] H. Liu, M. Niinomi, M. Nakai, K. Cho, Athermal and deformation-induced ω-phase transformations in biomedical beta-type alloy Ti-9Cr-0.2O, Acta Mater. 106 (2016) 162.
[7] K. Otsuka, X. Ren, Physical metallurgy of Ti-Ni-based shape memory alloys, Prog. Mater. Sci. 50 (2005) 511–678.
[8] S. Hanada, M. Ozeki, O. Izumi, Deformation characteristics in β phase Ti-Nb alloys, Metall. Trans. A 16A (1985) 789–795.
[9] D. Ping, Review on phase in body-centered cubic metals and alloys, Acta Metall. Sin. Engl. Lett. 27 (1) (2014) 1–11, http://dx.doi.org/10.1007/s40195-013-0014-2.
[10] P.J.S. Buenconsejo, H.Y. Kim, S. Miyazaki, Effect of ternary alloying elements on the shape memory behavior of Ti-Ta alloys, Acta Mater. 57 (2009) 2509–2515.
[11] H.Y. Kim, S. Hashimoto, J.I. Kim, T. Inamura, H. Hosoda, S. Miyazaki, Effect of Ta addition on shape memory behavior of Ti-22Nb alloy, Mater. Sci. Eng. A 417 (2006) 120–128.
[12] N.G. Jones, R.J. Dashwood, M. Jackson, D. Dye, β phase decomposition in Ti-5Al-5Mo-5V-3Cr, Acta Mater. 57 (2009) 3830.
[13] M.J. Lai, C.C. Tasan, J. Zhang, B. Grabowski, L.F. Huang, D. Raabe, Origin of shear induced β to ω transition in Ti-Nb-based alloys, Acta Mater. 92 (2015) 55.
[14] Z. Tarzimoghadam, S. Sandlöbes, K.G. Pradeep, D. Raabe, Microstructure design and mechanical properties in a near-α Ti-4Mo alloy, Acta Mater. 97 (2015) 291.
[15] P. Kwasniak, M. Muzyk, H. Garbacz, K.J. Kurzydlowski, Clustering of O-X, X=(Ag, Al, Ga, Sn, Sc, Zn, Zr) point defects in hexagonal Ti: formation mechanism and ductility variations, Mater. Chem. Phys. 154 (2015) 137.
[16] S.K. Sikka, Y.K. Vohra, R. Chidambaram, Omega phase in materials, Prog. Mater. Sci. 27 (1982) 245–310.
[17] T. Li, D. Kent, G. Sha, L.T. Stephenson, A.V. Ceguerra, S.P. Ringer, M.S. Dargusch, J.M. Cairney, New insights into the phase transformations to isothermal ω and ω-assisted α in near β-Ti alloys, Acta Mater. 106 (2016) 353.
[18] S. Miyazaki, H.Y. Kim, J.S. Buenconsejo, Development of high temperature Ti-Ta shape memory alloys, ESOMAT 2009 (2009) 01003.
[19] J.H. Dai, X. Wu, Y. Song, R. Yang, Electronic structure mechanism of martensitic phase transformation in binary titanium alloys, J. Appl. Phys. 112 (2012) 123718.
[20] B.E. Tegner, L. Zhu, G.J. Ackland, Relative strength of phase stabilizers in titanium alloys, Phys. Rev. B 85 (2012) 214106.
[21] S. Nag, R. Banerjee, R. Srinivasan, J.Y. Hwang, M. Harper, H.L. Fraser, ω-assisted nucleation and growth of α precipitates in the Ti-5Al-5Mo-5V-3Cr-0.5Fe β titanium alloy, Acta Mater. 57 (2009) 2136.
[22] A. Devaraj, R.E.A. Williams, S. Nag, R. Srinivasan, H.L. Fraser, R. Banerjee, Investigations of omega precipitation in titanium molybdenum alloys by

coupling 3d atom probe tomography and high resolution (S)TEM, Microsc. Microanal. 15 (2009) 268.
[23] D. Bhattacharyya, G.B. Viswanathan, R. Denkenberger, D. Furrer, H.L. Fraser, The role of crystallographic and geometrical relationships between α and β phases in an α/β titanium alloy,, Acta Mater. 51 (2003) 4679.
[24] H. Ikehata, N. Nagasako, T. Furuta, A. Fukumoto, K. Miwa, T. Saito, First-principles calculations for development of low elastic modulus Ti alloys, Phys. Rev. B 70 (2004) 174113.
[25] H. Ikehata, N. Nagasako, S. Kuramoto, T. Saito, Designing new structural materials using density functional theory: the example of gum metal,, MRS Bull. 31 (2006) 688–692.
[26] L. You, X. Song, First principles study of low young's modulus Ti-Nb-Zr alloy system, Mater. Lett. 80 (2012) 165–167.
[27] T. Li, J.W. Morris Jr., N. Nagasako, S. Kuramoto, D.C. Chrzan, Ideal engineering alloys, Phys. Rev. Lett. 98 (2007) 105503.
[28] R.J. Talling, R.J. Dashwood, M. Jackson, S. Kuramoto, D. Dye, Determination of $(c_{11}-c_{12})$ in Ti-36Nb-2Ta-3Zr-0.3O (wt.%) (gum metal), Scr. Mater. 59 (2008) 669–672.
[29] R.J. Talling, R.J. Dashwood, M. Jackson, D. Dye, Compositional variability in gum metal, Scr. Mater. 60 (2009) 1000–1003.
[30] J. Huang, H. Xing, J. Sun, Structural stability and generalized stacking fault energies in β Ti-Nb alloys: relation to dislocation properties, Scr. Mater. 66 (2012) 682–685.
[31] H. Xing, J. Sun, Q. Yao, W.Y. Guo, R. Chen, Origin of substantial plastic deformation in gum metals, Appl. Phys. Lett. 92 (2008) 151905.
[32] M. Tane, S. Akita, T. Nakano, K. Hagihara, Y. Umakoshi, M. Niinomi, H. Nakajima, Peculiar elastic behavior of Ti-Nb-Ta-Zr single crystals, Acta Mater. 56 (2008) 2856–2863.
[33] M. Tane, S. Akita, T. Nakano, K. Hagihara, Y. Umakoshi, M. Niinomi, H. Mori, H. Nakajima, Low young's modulus of Ti-Nb-Ta-Zr alloys caused by softening in shear moduli c′ and c_{44} near lower limit of body-centered cubic phase stability, Acta Mater. 58 (2010) 6790–6798.
[34] M. Tane, T. Nakano, S. Kuramoto, M. Hara, M. Niinomi, N. Takesue, T. Yano, H. Nakajima, Low young's modulus of Ti-Nb-Ta-Zr alloys: cold working and oxygen effects, Acta Mater. 59 (2011) 6975–6988.
[35] Y.W. Zhang, S.J. Li, E.G. Obbard, H. Wang, S.C. Wang, Y.L. Hao, R. Yang, Elastic properties of Ti-24Nb-4Zr-8Sn single crystals with bcc crystal structure, Acta Mater. 59 (2011) 3081–3090.
[36] Z.G. Mei, S.L. Shang, Y. Wang, Z.K. Liu, Density-functional study of the thermodynamic properties and the pressure-temperature phase diagram of ti, Phys. Rev. B 80 (2009) 104116.
[37] C.-E. Hu, Z.-Y. Zeng, L. Zhang, X.-R. Chen, L.-C. Cai, D. Alfé, Theoretical investigation of the high pressure structure, lattice dynamics, phase transition, and thermal equation of state of titanium metal, J. Appl. Phys. 107 (9) (2010) 093509.
[38] R.G. Hennig, D.R. Trinkle, J. Bouchet, S.G. Srinivasan, R.C. Albers, J.W. Wilkins, Impurities block the alpha to omega martensitic transformation in titanium, Nat. Mater. 4 (2005) 129–133.
[39] R.G. Hennig, T.J. Lenosky, D.R. Trinkle, S.P. Rudin, J.W. Wilkins, Classical potential describes martensitic phase transformations between the α, β, and ω titanium phases, Phys. Rev. B 78 (2008) 054121.
[40] L.-F. Huang, B. Grabowski, E. McEniry, D.R. Trinkle, J. Neugebauer, Importance of coordination number and bond length in titanium revealed by electronic structure investigations, Phys. Status Solidi B 252 (2015) 1907.
[41] J. Hafner, Ab-initio simulations of materials using vasp: density-functional theory and beyond, J. Comput. Chem. 29 (2008) 2044–2078.
[42] P.E. Blöchl, Projector augmented-wave method, Phys. Rev. B 50 (1994) 17953–17979, http://dx.doi.org/10.1103/PhysRevB.50.17953.
[43] G. Kresse, D. Joubert, From ultrasoft pseudopotentials to the projector augmented-wave method, Phys. Rev. B 59 (1999) 1758–1775, http://dx.doi.org/10.1103/PhysRevB.59.1758.
[44] J.P. Perdew, K. Burke, M. Ernzerhof, Generalized gradient approximation made simple, Phys. Rev. Lett. 77 (1996) 3865–3868, http://dx.doi.org/10.1103/PhysRevLett.77.3865.
[45] M. Methfessel, A.T. Paxton, High-precision sampling for brillouin-zone integration in metals, Phys. Rev. B 40 (1989) 3616–3621, http://dx.doi.org/10.1103/PhysRevB.40.3616.
[46] N.D. Mermin, Thermal properties of the inhomogeneous electron gas, Phys. Rev. 137 (1965) A1441.
[47] V.L. Moruzzi, J.F. Janak, K. Schwarz, Calculated thermal-properties of metals, Phys. Rev. B 37 (1988) 790–799.
[48] D. Raabe, B. Sander, M. Friák, D. Ma, J. Neugebauer, Theory-guided bottom-up design of β-titanium alloys as biomaterials based on first principles calculations: theory and experiments, Acta Mater. 55 (2007) 4475–4487.
[49] P. Lazar, M. Jahnátek, J. Hafner, N. Nagasako, R. Asahi, C. Blaas-Schenner, M. Stöhr, R. Podloucky, Temperature-induced martensitic phase transitions in gum-metal approximations: first-principles investigations for ti_3 nb, Phys. Rev. B 84 (2011) 054202.
[50] F.R. de Boer, R. Boom, A.R. Miedema, Enthalpies of formation of liquid and solid binary alloys based on 3d metals, Phys. B+C 101 (1980) 294.
[51] V.L. Moruzzi, A.R. Williams, J.F. Janak, Local density theory of metallic cohesion, Phys. Rev. B 15 (1977) 2854.
[52] M.S.S. Brooks, B. Johansson, Exchange integral matrices and cohesive energies of transition metal atoms, J. Phys. F. Met. Phys. 13 (1983) L197–L202.
[53] J.H. Rose, H.B. Shore, Bonding energetics of metals: explanation of trends, Phys. Rev. B 43 (1991) 11605–11611.
[54] P.H.T. Philipsen, E.J. Baerends, Cohesive energy of 3d transition metals: density functional theory atomic and bulk calculations, Phys. Rev. B 54 (1996) 5326–5333.
[55] S.L. Shang, A. Saengdeejing, Z.G. Mei, D.E. Kim, H. Zhang, S. Ganeshan, Y. Wang, Z.K. Liu, First-principles calculations of pure elements: equations of state and elastic stiffness constants, Comput. Mater. Sci. 48 (2010) 813–826.
[56] A.P. Sutton, Electronic Structure of Materials, Oxford University Press, Oxford, 1993.
[57] G.A. Landrum, R. Dronskowski, The orbital origins of magnetism: from atoms to molecules to ferromagnetic alloys, Angew. Chem. Int. Ed. 39 (2000) 1560–1585.
[58] Y.L. Hao, S.J. Li, S.Y. Sun, R. Yang, Effect of Zr and Sn on young's modulus and superelasticity of Ti-Nb-based alloys, Mater. Sci. Eng. A 441 (2006) 112–118.
[59] S. Miyazaki, H.Y. Kim, H. Hosoda, Development and characterization of Ni-free Ti-base shape memory and superelastic alloys, Mater. Sci. Eng. A 438 – 440 (2006) 18–24.
[60] Y.L. Hao, S.J. Li, F. Prima, R. Yang, Controlling reversible martensitic transformation in titanium alloys with high strength and low elastic modulus, Scr. Mater. 67 (2012) 487–490.
[61] D. de Fontaine, Simple models for the omega phase transformation, Metall. Trans. A 19A (1988) 169–175.
[62] D.L. Moffat, D.C. Larbalestier, The competition between martensite and omega in quenched Ti-Nb alloys, Metall. Trans. A 19A (1988) 1677–1686.
[63] T. Ahmed, H.J. Rack, Martensitic transformations in Ti–(16–26 at%) Nb alloys, J. Mater. Sci. 31 (1996) 4267–4276.
[64] H.Y. Kim, Y. Ikehara, J.I. Kim, H. Hosoda, S. Miyazaki, Martensitic transformation, shape memory effect and superelasticity of Ti-Nb binary alloys, Acta Mater. 54 (2006) 2419–2429.
[65] A. Devaraj, S. Nag, R. Srinivasan, R.E.A. Williams, S. Banerjee, R. Banerjee, H.L. Fraser, Experimental evidence of concurrent compositional and structural instability leading to ω precipitation in titanium-molybdenum alloys, Acta Mater. 60 (2011) 596–609.
[66] T. Saito, T. Furuta, J.H. Hwang, S. Kuramoto, K. Nishino, N. Suzuki, R. Chen, A. Yamada, K. Ito, Y. Seno, T. Nonaka, H. Ikehata, N. Nagasako, C. Iwamoto, Y. Ikuhara, T. Sakuma, Multifunctional alloys obtained via a dislocation-free plastic deformation mechanism, Science 300 (2003) 464–467.
[67] S. Kuramoto, T. Furuta, J.H. Hwang, K. Nishino, T. Saito, Plastic deformation in a multifunctional Ti-Nb-Ta-Zr-O alloy, Metall. Trans. A 37A (2006) 657.
[68] T. Furuta, S. Kuramoto, J. Hwang, K. Nishino, T. Saito, Elastic deformation behavior of multi-functional Ti-Nb-Ta-Zr-O alloys, Mater. Trans. 46 (2005) 3001–3007.
[69] R.J. Talling, R.J. Dashwood, M. Jackson, D. Dye, On the mechanism of superelasticity in gum metal, Acta Mater. 57 (2009) 1188–1198.
[70] E. Plancher, C.C. Tasan, S. S, D. Raabe, On dislocation involvement in Ti-Nb gum metal plasticity, Scr. Mater. 68 (2013) 805–808.
[71] M.Y. Gutkin, T. Ishizaki, S. Kuramoto, I.A. Ovidko, Nanodisturbances in deformed gum metal, Acta Mater. 54 (2006) 2489–2499.
[72] H. Xing, W.Y. Guo, J. Sun, Substructure of recovered Ti-23Nb-0.7Ta-2Zr-O alloy, Trans. Nonferr. Met. Soc. China 17 (2007) 1456–1458.
[73] Y. Yang, S.Q. Wu, G.P. Li, Y.L. Li, Y.F. Lu, K. Yang, P. Ge, Evolution of deformation mechanisms of Ti-22.4Nb-0.73Ta-2Zr-1.34O alloy during straining, Acta Mater. 58 (2010) 2778–2787.
[74] P. Castany, M. Besse, T. Gloriant, Dislocation mobility in gum metal β-titanium alloy studied via in situ transmission electron microscopy, Phys. Rev. B 84 (2011) 020201(R).
[75] M. Besse, P. Castany, T. Gloriant, Mechanisms of deformation in gum metal TNTZ-O and TNTZ titanium alloys: a comparative study on the oxygen influence,, Acta Mater. 59 (2011) 5982–5988.
[76] H. Xing, J. Sun, Mechanical twinning and omega transition by <111>{ 112} shear in a metastable β titanium alloy, Appl. Phys. Lett. 93 (2008) 031908.
[77] Y. Yang, G.P. Li, G.M. Cheng, H. Wang, M. Zhang, F. Xu, K. Yang, Stress-introduced α'' martensite and twinning in a multifunctional titanium alloy, Scr. Mater. 58 (2008) 9–12.
[78] E. Withery, M. Jin, A. Minor, S. Kuramoto, D.C. Chrzan, J.W. Morris Jr., The deformation of gum metal in nanoindentation, Mater. Sci. Eng. A 493 (2008) 26–32.
[79] E.A. Withery, A.M. Minor, D.C. Chrzan, J.W. Morris Jr., S. Kuramoto, The deformation of gum metal through in situ compression of nanopillars, Acta Mater. 58 (2010) 2652–2665.
[80] Y. Yang, G.P. Li, G.M. Cheng, Y.L. Li, K. Yang, Multiple deformation mechanisms of Ti-22.4Nb-0.73Ta-2.0Zr-1.34O alloy, Appl. Phys. Lett. 94 (2009) 061901.
[81] S. Hanada, A. Takemura, O. Izumi, The mode of plastic deformation of β Ti-V alloys, Trans. Jpn. Inst. Metals 23 (1982) 507–517.
[82] S. Hanada, O. Izumi, Correlation of tensile properties, deformation modes, and phase stability in commercial β-phase titanium alloys, Metall. Trans. A 18A (1987) 265–271.
[83] D.C. Chrzan, M.P. Sherburne, Y. Hanlumyuang, T. Li, J.W. Morris Jr., Spreading of dislocation cores in elastically anisotropic body-centered-cubic materials: the case of gum metal, Phys. Rev. B 82 (2010) 184202.
[84] S.V. Bobylev, T. . ishizaki, S. Kuramoto, I.A. Ovidko, Theory of the nonplanar splitting of screw dislocations in gum metal, Phys. Rev. B 77 (2008) 094115.